

Primary insights into the superconducting twin qubit

I. V. Antonov

*Royal Holloway, University of London, Egham, TW20 0EX, UK and
National Physical Laboratory, Hampton Road Teddington, TW11 0LW, UK*

R. S. Shaikhaidarov

Royal Holloway, University of London, Egham, TW20 0EX, UK

V. N. Antonov

*Royal Holloway, University of London, Egham, TW20 0EX, UK
Skolkovo Institute of Science and Technology, Nobel str. 3, Moscow, 143026, Russia and
Moscow Institute of Physics and Technology, 29 Institutskiy per.,
141700 Dolgoprudny, Moscow Region, Russia*

O.V. Astafiev

*Royal Holloway, University of London, Egham, TW20 0EX, UK
Skolkovo Institute of Science and Technology, Nobel str. 3, Moscow, 143026, Russia and
National Physical Laboratory, Hampton Road Teddington, TW11 0LW, UK*

(Dated: May 9, 2019)

Short decoherence times stand as one of the main obstacles hindering industrial scale implementation of quantum processors based on superconducting qubits. The simplicity and flexibility of fabricating superconducting qubits compared with other qubit architectures, most notably trapped ions, has to be set against their limited ability of handling sequential state operations - the most successful processor prototype has a decoherence time of $\sim 60\ \mu\text{s}$ while the gate operation time is about $20\ \mu\text{s}$ [1]. Therefore, within 3 gate operations it's quantum state becomes substantially deteriorated.

In this work we look at increasing the qubit's decoherence time using a new geometry - a fusion of two flux qubits joined by a common Josephson Junction. At the degeneracy flux-bias point, $\frac{1}{2}\Phi_0$, the twin qubit is measured to have energy spectrum plateaus with curvature several orders of magnitude lower than that in the usual flux qubits. This flatness makes the qubit more robust to flux noise. Also, the new qubit allows $|1\rangle \leftrightarrow |2\rangle$ dipole transition, forbidden in other qubit designs. We experimentally study the new qubit, measure the transmission spectrum, Rabi oscillations, and simulate dipole transitions of the qubit. Potentially the new qubit may outperform the current mainstream design.

I. INTRODUCTION

Superconducting qubits are one of the promising trends for implementing quantum computing technology. Being nothing more than strips of aluminum on a chip, their geometry can be designed to select an operating energy, state transition rates and sensitivity that would fit the use-case of very specific environments. Over the past decade they have been carried out the functionality of a transistor [4][5], where a control field was used to pass or block a second field at a different frequency, multiplexer [6], 2 input signals can be mixed to controllably generates a single output signal, and serial bus [7]. Superconducting qubits can be produced using industry standard nanofabrication techniques and integrated at scale into large coherent circuits [8]. All speaks to a strong case of servicing future quantum electronic platforms with this technology.

One of the inherent limitation superconducting qubits face is a comparatively short coherence time,

τ_{dec} , after which quantum information becomes lost, (Appendix A). For example, the transmon qubits in the revolutionary 5-qubit quantum experience from IBM (research.ibm.com/ibm-q) have a coherence time of $\sim 60\ \mu\text{s}$ [1]. For reference, qubits on trapped ${}^+{}^{\text{Be}}{}^9$ ions had a coherence time of $\sim 1\ \text{ms}$ over 20 years ago [9]. In order to have a sufficient number of quantum logic operations for multi-stage computations, say 10^4 , coherence times need to surpass the $100\ \mu\text{s}$ barrier [11].

Strong decoherence in superconducting qubits is a consequence of the large capacitances inherent to their geometry. The loop of the flux qubits are typically $1\ \mu\text{m}$ or greater in size [4][5][8], which couples them to charge variations in the external environment. The charge fluctuations in the environment result in random changes of the qubit's energy levels and, consequently, to an erratic evolution of the quantum state that 'averages' out information on the off-diagonal elements of the density matrix [10].

Flux qubit architectures have been developed to

address this decoherence problem by making the energy of the Josephson junctions (JJ) dominate over the charging energy, $E_J/E_C \gg 1$, which lowers the device's charge sensitivity [11] [12] [13]. A whole family of flux qubit designs have lead to improvement of the coherence times: quantronium ~ 500 ns [14] [15], shunted phase qubit $\sim 10\ \mu\text{s}$ [16], shunted flux qubit $\sim 80\ \mu\text{s}$ [17], 4-JJ qubit [18], fluxonium $\sim 1\ \text{ms}$ [19].

We extended this list with a ‘twin’ qubit, consisting of two symmetrical flux qubits, linked by a common α -Josephson Junction (Fig. 1). A chain of 15 such qubits was recently placed into a coplanar waveguide to demonstrate flux-tunable transmission of microwaves [21]. Of particular interest to us was the weak flux dependence of the systems transition energy when it was biased to the degeneracy point $\frac{1}{2}\Phi_0$, making it benefit from both low flux and charge sensitivities.

In this work we isolate one of these twin qubits and provide experimental evidence for: strong anharmonicity with respect to the $|1\rangle \leftrightarrow |2\rangle$ and $|2\rangle \leftrightarrow |3\rangle$ transitions; weak flux dependence of the transition energies close to the degeneracy point; compliance of experimental data with simulations of the energy structure and controllability of the $|1\rangle \leftrightarrow |2\rangle$ transition rate.

II. FABRICATION

The qubits and transmission line are fabricated on an undoped 100 silicon substrate, which is pre-patterned with 10 nm NiCr - 90 nm Au ground planes and markers. We begin by cleaning the wafer for ~ 10 minutes at 60 C in acetone rinsing in de-ionized water. Two layers of electron resist are sequentially spun and post baked (3 minutes at 60 C) onto the wafer: Copolymer 13%, 700 nm; ZEP520a:Anisole 2:1, 60 nm. We use an electron beam lithographer to expose the resist using a 30 kV, 10 pA beam delivering a dose of $70\ \mu\text{C}/\text{cm}^2$. We develop the pattern in Pylxylen for 35 seconds followed by a 5 minute submersion in Isopropanol:H₂O 93:7 and rinse in pure Isopropanol. Shadow evaporation of aluminum in a Plassys [22] simultaneously deposits the JJs and the transmission line. Dry etching with argon removes oxide layers for good galvanic contact to the gold pattern, and, maintaining high vacuum, we deposit 20 nm of Al and perform static oxidation for 10 minutes at 0.3 mBar to generate the intermediate AlO_x insulating barrier for the JJ. A second 30 nm layer of Al completes the process.

These steps give us the 5-JJ structure of the twin qubits. Qubits are capacitively coupled to the trans-

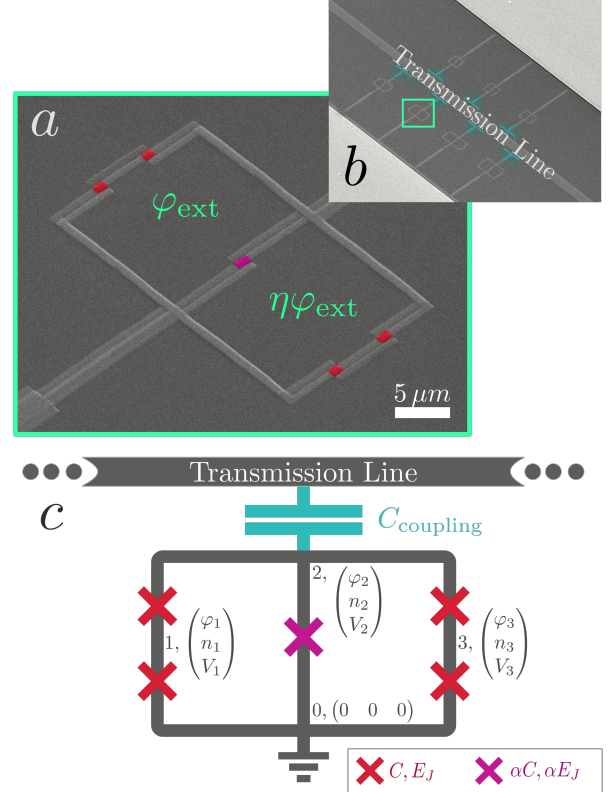


FIG. 1. **Geometry of a twin qubit:** a) Scanning electron microscope image of the qubit flux with phase biases φ , $\eta\varphi$ applied to its superconducting loops. The repeated line structures are the by-product of the double-angle evaporation of aluminum that creates the Al-AlO_x-Al JJs highlighted in red and pink; b) Each of the qubits is coupled to the transmission line with a T-shaped capacitor; c) The twin qubit is a symmetrical arrangement of two individual flux qubits (as described in [11]) sharing the central JJ. Islands are labeled with a Cooper pair occupation n_i , phase φ_i and voltage V_i , with the ground setting a reference of 0 for all three variables. JJs (marked with crosses) mediate capacitive and Josephson interactions between the islands. The central junction has a capacitance of αC and an energy αE_J , compared with the C_J , E_J values of the outside ones.

mission line through and T-shaped capacitors them to the transmission line, see Fig. 1. Each JJ has an area of $400 \times 200\ \text{nm}^2$. The coplanar transmission line with impedance $Z_0 \sim 50\ \Omega$ runs to the opening between the ground planes in the center of the chip.

We bond the sample chip to a printed circuit board and mount it on a holder with a niobium-coil magnet on the 13 mK stage of a dilution refrigerator. A superconducting cover is used to shield the holder from stray magnetic fields. The RF lines running to the sample have attenuators, -50 dBm on the 50 K stage, -30 dBm on the 4 K stage, thermalize the in-

put lines. We attach a circulator on the output line for isolation. The transmitted signal is amplified by +35 dBm on the 4K stage and by +35 dBm at room temperature. This set of attenuators and amplifiers facilitate power conversion between the laboratory equipment and qubit microwaves. We surround each temperature stage of the system with a reflective cover, that thermally shields from higher stages. Prior to performing characterization measurement, we took the microwave transmission spectrum with the qubit detuned, and corrected all further measurements by the background transmission profile.

In this experiment did not go to the depths of chemical and physical treatment of the substrate surface to remove two-level system defects in the silicon oxide layer [23] or employing infra-red filters to eliminate stray light during measurement [24]. Rather we concentrate on revealing the intrinsic potential of the twin qubit design and the weaknesses that will have to be addressed in the future.

III. OPERATIONS WITH QUBITS

We record the energy spectrum of the twin qubit while sweeping the biasing magnetic flux. Because of a small asymmetry, η , the fluxes linked through the left and right loops are $\Phi = \frac{\varphi}{2\pi}\Phi_0$ and $\eta\Phi$.

The $|1\rangle \leftrightarrow |2\rangle$ transition, ω_{21} , is mapped with a network analyzer, which measures the transmission of signal ω_{NA} through the system. Away from resonance the signal passes through the circuit without any interaction with the qubit. After correcting for line losses, transmission is close to 100%. Only near resonance ($\omega_{NA} = \omega_{21}$), does the qubit exchange photons with the driving field as it evolves between the ground and excited states [1]. The qubit emits a wave that is exactly in anti-phase with the driving field [25], and the destructive superposition in the output line results in a transmission dip, see Fig. 2. The bottom of this dip is marked with blue circles. The trace of circles at different magnetic flux maps out the qubit's ω_{21} transition spectrum, see inset of Fig. 2.

The $|2\rangle \leftrightarrow |3\rangle$ transition, ω_{32} , is mapped using two-tone spectroscopy. The network analyzer is tuned to the transition frequency ω_{21} , taken from the first measurement and called the probe signal, while an additional generator sweeps a second frequency, ω_{GEN} . Whenever the generator strikes the $|2\rangle \rightarrow |3\rangle$ transition ($\omega_{GEN} = \omega_{32}$), the qubit undergoes a ladder of excitations, $|1\rangle \xrightarrow{\omega_{21}} |2\rangle \xrightarrow{\omega_{32}} |3\rangle$, depopulating states $|1\rangle$ and $|2\rangle$. Because of this depopulation, the probe signal becomes less involved with driving and it's transmission moves out of the dip in Fig. 2. This

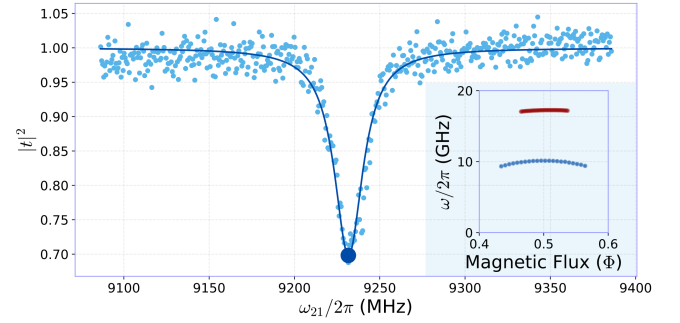


FIG. 2. Mapping the qubit transition spectrum: For the lower transition ω_{21} (blue, inset) a network analyzer measures the power transmission coefficient, $|t|^2$, at flux bias Φ and microwave frequency $\omega_{21}/2\pi$. A Lorentzian fit [4] to the transmission profile establishes the resonant frequency, which is marked with blue points on the flux-frequency spectrum. For transition ω_{32} (red, inset) a two-tone measurement is run by monitoring changes to a weak ω_{21} probe while sweeping a second frequency in search of the higher transition.

identifies ω_{32} which is mapped with red circles in the transition energy-magnetic field spectrum.

We match the experimental data points to simulations made on the standard Hamiltonian, $\mathcal{H} = T + U$ [11]. Islands, isolated by the JJ in Fig. 1, are labeled with Cooper pair (CP) occupation $\vec{n} = |n_1, n_2, n_3\rangle$, phase $\vec{\varphi} = |\varphi_1, \varphi_2, \varphi_3\rangle$ and voltage $\vec{V} = |V_1, V_2, V_3\rangle$ states. The charges and voltages on the islands are linked by the capacitance matrix

$$2e\vec{n} = \hat{C}\vec{V}$$

where the capacitance matrix in the topology of Fig. 1 is

$$\hat{C} = |C| \begin{pmatrix} 2 & -1 & 0 \\ -1 & 2 + \alpha & -1 \\ 0 & -1 & 2 \end{pmatrix},$$

where $|C|$ is the capacitance of the outer JJs. The interaction of the CPs, carrying a charge $\vec{Q} = 2e\vec{n}$, and voltages on their respective islands gives rise to the ‘kinetic’ term of the Hamiltonian:

$$\begin{aligned} T &= \frac{1}{2} \sum_{i=1}^3 Q_i V_i = \frac{(2e)^2}{2} \vec{n} \hat{C}^{-1} \vec{n}^T \\ &= E_C |C| \langle \hat{C}^{-1} \rangle_{|n_1, n_2, n_3\rangle}, \end{aligned}$$

where we define $E_C = (2e)^2/2|C|$.

Each JJ with a phase difference of $\Delta\varphi_i$, contributes a ‘potential’ energy of $E_{Ji}(1 - \cos(\Delta\varphi_i))$.

The flux quantization condition for the left and right loops, $\sum_i^{\text{loop}} \varphi_i = 2\pi n, n \in \mathbb{Z}$, enters as a dependence on φ_{ext} and $\eta\varphi_{\text{ext}}$ on two of the junctions:

$$U = E_J [4 + \alpha - \alpha \cos(\varphi_2) - \cos(\varphi_1) - \cos(\varphi_3) - \cos(\varphi_2 - \varphi_1 - \varphi_{\text{ext}}) - \cos(\varphi_2 - \varphi_3 + \eta\varphi_{\text{ext}})].$$

The Hamiltonian is solved in the CP-basis, \vec{n} , where it's matrix representation takes the form shown in Fig. 3. The basis consists of elements such as $| -1, 0, 1 \rangle$, representing the CP occupation of the three islands. In the matrix shown each island can have an occupation $-1 \leq n_i \leq 1$ (3 CP states), for a total of 27 system states. In the simulation, this was increased to 343 by using 7 CP states. Kinetic terms (T) naturally fall on the diagonal axis of the matrix. Potential terms (U) are expanded to complex exponentials, which become off diagonal elements - see derivation in Appendix B. For example $\cos(\varphi_2)$ becomes $\mathbb{I}_1 \otimes \frac{1}{2} [\sum_{n_2} |n_2+1\rangle \langle n_2| + |n_2-1\rangle \langle n_2|] \otimes \mathbb{I}_3$, where identity operators $\mathbb{I}_{1,3}$ carry the states of the non-involved islands.

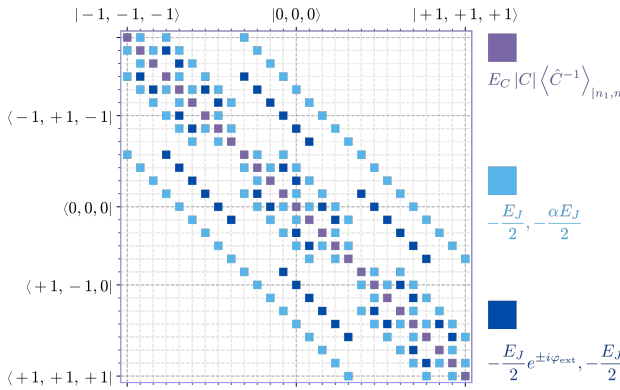


FIG. 3. Hamiltonian in the CP-basis representation: Purple square denote the kinetic terms that all fall on the main diagonal. Light blue squares denote simple off-diagonal terms, distributed symmetrically about the main diagonal. Dark blue squares are have an additional flux dependence of the forms $e^{i\varphi_{\text{ext}}}, e^{i\eta\varphi_{\text{ext}}}$.

The eigenenergies of the resulting Hamiltonian are compared with the experimental data in Fig. 4 using $E_J = 91.0 \text{ GHz}$, $E_C = 13.50 \text{ GHz}$, $\alpha = 1.023$, $\eta = 1.011$. Readings for ω_{32} are in a narrow flux range because away from $\Phi = (n + \frac{1}{2})\Phi_0, n \in \mathbb{Z}$, it gets harder to tune the VNA to ω_{21} (as part of the two-tone spectroscopy procedure) which prevents the accurate mapping of ω_{32} with the second tone. The asymmetry value, η , is close to the visual loop area difference of 3% seen from the SEM image in Fig. 1. The resonance is periodic in flux, with a tendency of higher ω_{21} at higher magnetic flux numbers.

An important qubit parameter is the curvature

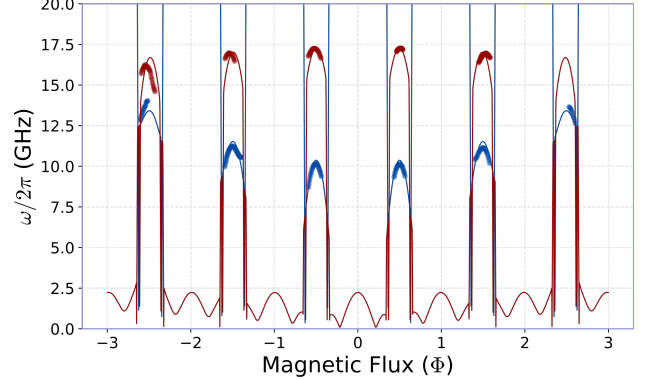


FIG. 4. Experimental spectra, circles, and simulation, solid lines, of the twin qubit: Shown are the transition frequencies ω_{21} (blue) and ω_{32} (red). Asymmetry in the flux penetrating the left and right loops results in the gradual change of transition frequencies with every Φ_0 period - ω_{21} creeps up, while ω_{32} creeps down, breaking the usual spectrum periodicity of flux qubits.

at the turning points in the energy spectrum, at the operation point of the qubit. A low curvature is desirable, to make the qubit less sensitive to external flux changes, which would improve decoherence time. At the twin qubits' degeneracy points $\Phi = (n + \frac{1}{2})\Phi_0, n \in \mathbb{Z}$, the curvature is $-550 \pm 10 \text{ GHz}/\Phi_0^2$. It is substantially smaller than $13 \times 10^4 \text{ GHz}/\Phi_0^2$ on the 4-JJ flux qubit [16], 8.4×10^4 [20] and $37 \times 10^4 \text{ GHz}/\Phi_0^2$ [29] on the 3-JJ flux qubits demonstrated recently. The decoherence time of $= 42 \text{ ns}$, taken with Rabi oscillation in Fig. 5 and described in Appendix C, was however relatively short. We attribute this to poisoning of the sample with the infrared radiation, and simplified technology used for the qubit's fabrication.

IV. DIPOLE TRANSITION

Finally we characterize the dipole moment of the twin qubit for between the lowest two states, $|1\rangle$ and $|2\rangle$. Microwaves in the transmission line, carrying a voltage $V_{mw} = |V_{mw}| \cos(\omega_{21}t)$, are coupled via capacitor C_{coupling} to the qubit, inducing a charge $Q_2 = C_{\text{coupling}} V_{mw}$ on island 2. $|1\rangle \leftrightarrow |2\rangle$ transitions stimulated by this driving, set up a qubit voltage of $\delta V_2 = \langle 1 | \hat{V}_{20} | 2 \rangle$ between the ground island and island 2 and hence draw an electrostatic energy related to the strength of the drive Ω

$$\begin{aligned} \delta V_2 Q_2 &= \langle 1 | \hat{V}_{20} | 2 \rangle C_{\text{coupling}} |V_{mw}| \cos(\omega_{21}t) \\ &= \hbar \Omega \cos(\omega_{21}t). \end{aligned}$$

Thus, the evaluation of $\langle 1 | \hat{V}_{20} | 2 \rangle =$

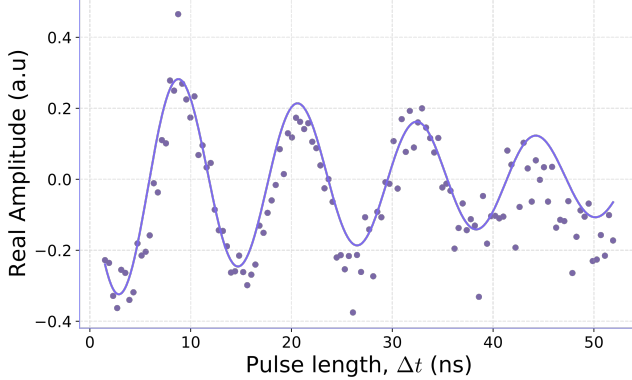


FIG. 5. Rabi oscillation taken at the degeneracy point by driving the qubit with resonant microwaves pulses for fixed time periods, Δt . The decoherence time of $\tau_{\text{dec}} = 42 \text{ ns}$ is extracted from the decay envelope, $e^{-\Delta t/\tau_{\text{dec}}}$, of the the oscillations.

$\langle 1 | \frac{E_C}{2|e|(1+\alpha)} [\hat{n}_1 + 2\hat{n}_2 + \hat{n}_3] | 2 \rangle$ gives, up to some constants of proportionality, the coupling strength that can be achieved with the twin qubit system at different values of the magnetic field.

To quantitatively compare coupling strength with other types of flux qubit geometries, we re-express this voltage element through flux:

$$\begin{aligned} \langle 1 | \hat{V}_2 | 2 \rangle &= \frac{d}{dt} \langle 1 | \hat{\Phi} | 2 \rangle \\ &= \frac{d}{dt} \left[\left(e^{i\omega_{21}t/2} \langle 1 \rangle \right) \hat{\Phi} \left(e^{+i\omega_{21}t/2} | 2 \rangle \right) \right] \\ &= i\omega_{21}\beta\Phi_0, \end{aligned}$$

where we have used the free evolution of a 2-level system, $U(t) = e^{-i\frac{\mathcal{H}}{\hbar}t}$, $\mathcal{H} = -\frac{\hbar\omega_{21}}{2}\sigma_z$, to draw out the time-dependent phases in the second line of calculation. $\beta = \langle 1 | \hat{\Phi} | 2 \rangle / \Phi_0$ is the normalized coupling constant, that can be compared across geometries.

In Fig. 6, β is compared between our twin qubit and a 4-JJ flux qubit [6]. Irrespective of the energies used in the simulations, the twin qubit always has a local maximum of coupling strength at degeneracy points $\Phi = (n + \frac{1}{2})\Phi_0$, $n \in \mathbb{Z}$, while the 4-JJ coupling strength goes to zero. Earlier we discussed the benefits of operating qubits near degeneracy points, where there is a low magnetic field sensitivity. The twin qubit has the feature of supporting $|1\rangle \leftrightarrow |2\rangle$ transitions at these optimal working points - transitions which are forbidden for other geometries.

V. CONCLUSION

We have fabricated and characterized the first isolated twin qubit, the distinguishing features

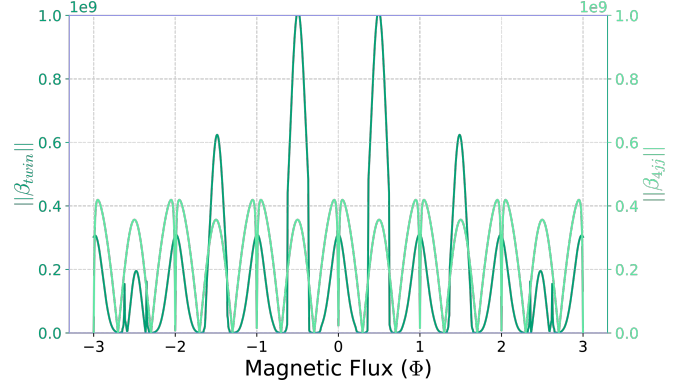


FIG. 6. **Dipole transition spectrum:** The element $\langle 1 | \hat{V}_2 | 2 \rangle$ is evaluated using the flux-dependent eigenstates $|1\rangle$, $|2\rangle$ of the system's Hamiltonian and normalized to $\beta = \frac{\langle 1 | \hat{V}_2 | 2 \rangle}{i\omega_{21}\Phi_0}$. Plotted is the absolute magnitude $\|\beta\|$, which carries real and imaginary components. For the twin qubit we use the $E_J = 91.0 \text{ GHz}$, $E_C = 13.50 \text{ GHz}$, $\alpha = 1.023$, $\eta = 1.011$ found earlier in the paper, while for the 4-JJ flux qubit we use $E_C = 20 \text{ GHz}$, $E_J = 30 \text{ GHz}$, $\alpha = 0.45$. The operating regions the qubits lie around degeneracy points $\Phi = (n + \frac{1}{2})\Phi_0$, $n \in \mathbb{Z}$, where the 4-JJ flux qubit has a forbidden $|1\rangle \leftrightarrow |2\rangle$ transition, signified by a vanishing β .

of which are the weak flux sensitivity and allowed $|1\rangle \leftrightarrow |2\rangle$ transitions at degeneracy points $\Phi = (n + \frac{1}{2})\Phi_0$, $n \in \mathbb{Z}$, compared to other flux qubit geometries. Improved fabrication techniques can further advance the qubit's decoherence time to place it in competition of serving as enhanced building block in quantum electronic circuits.

Appendices

A. DECOHERENCE RESULTS IN LOSS OF QUANTUM INFORMATION

Quantum processing involves manipulating the state of a qubit, Ψ , changing the relative state population, $|\alpha| \leq 1$, and phase, φ , between states $|0\rangle$ and $|1\rangle$:

$$\Psi = \alpha | 0 \rangle + e^{i\varphi}(1 - \alpha) | 1 \rangle.$$

When written as a density matrix, the phase information is mapped onto the off-diagonal elements:

$$\rho = |\Psi\rangle \langle \Psi| = \begin{pmatrix} |\alpha|^2 & \alpha(1 - \alpha)e^{-i\varphi} \\ \alpha(1 - \alpha)e^{+i\varphi} & |(1 - \alpha)|^2 \end{pmatrix}$$

Decoherence, by definition, causes the off-diagonal elements decay to $1/e$ of the initial value, over a time period τ_{dec} , and computational information encoded in phase φ becomes lost.

B. EXPANSION OF POTENTIAL TERM, U , IN THE CP-BASIS

Switching to the CP-basis, leads to a non-trivial representation of phase-dependent terms in the potential, $U(\varphi_1, \varphi_2, \varphi_3, \varphi_{\text{ext}})$. The following explanation will illustrate the expansion process for $\cos(\varphi_2)$.

Using the commutation relation for conjugate number and phase operators $[\hat{n}, \hat{\phi}] = 1$, we arrive at the result

$$\begin{aligned} [\hat{n}, e^{\pm i\hat{\phi}}] &= \left[\hat{n}, \sum_{\alpha=0}^{\infty} \frac{(\pm i\hat{\phi})^\alpha}{\alpha!} \right] = \sum_{\alpha=0}^{\infty} (\pm i)^\alpha \frac{[\hat{n}, \hat{\phi}^\alpha]}{\alpha!} \\ &= \sum_{\alpha=0}^{\infty} (\pm i)^\alpha \frac{-\alpha i\hat{\phi}^{\alpha-1}}{\alpha!} = \pm \sum_{\alpha=1}^{\infty} i^{\alpha-1} \frac{(\pm \hat{\phi})^{\alpha-1}}{(\alpha-1)!} = \pm e^{\pm i\hat{\phi}}, \end{aligned}$$

Operating with the number operator on the state $e^{\pm i\hat{\phi}}|n\rangle$ and substituting in the previous commutation result yields

$$\hat{n} \left[e^{\pm i\hat{\phi}} |n\rangle \right] = \left[\pm e^{\pm i\hat{\phi}} + e^{\pm i\hat{\phi}} \hat{n} \right] |n\rangle = (n \pm 1) \left[e^{\pm i\hat{\phi}} |n\rangle \right],$$

meaning that the exponential phase operator is a ladder operator for the $|n\rangle$ state:

$$e^{\pm i\hat{\phi}} |n\rangle = |n \pm 1\rangle \Rightarrow e^{\pm i\phi} = \sum_i |n_i \pm 1\rangle \langle n_i|.$$

Now phase a φ_2 operator can be expressed in the

number basis as follows:

$$\cos(\varphi_2) = \frac{1}{2} \left(e^{i\varphi_2} + e^{-i\varphi_2} \right) = \frac{1}{2} \left(\sum_i |n_i^{(2)} \pm 1\rangle \langle n_i^{(2)}| \right) \otimes \mathbb{I}^{(1)} \otimes \mathbb{I}^{(3)}$$

with $\mathbb{I}^{(1)} = \sum_i |n_i^{(1)}\rangle \langle n_i^{(1)}|$ and $\mathbb{I}^{(3)} = \sum_i |n_i^{(3)}\rangle \langle n_i^{(3)}|$ being the identity operators in the $n^{(1)}$ and $n^{(3)}$ subspaces.

C. RABI OSCILLATION MEASUREMENTS

The Hamiltonian during driving is a combination of the qubit's two-level system

$$\mathcal{H}_q = -\frac{\hbar\omega_{21}}{2} \sigma_z,$$

where $\sigma_z = \begin{pmatrix} 1 & 0 \\ 0 & -1 \end{pmatrix}$, and the resonant drive of strength $\hbar\Omega$

$$\mathcal{H}_d = \hbar\Omega \cos(\omega_{21}t) \sigma_x$$

that couples the two levels through the transition operator $\sigma_x = \begin{pmatrix} 0 & 1 \\ 1 & 0 \end{pmatrix}$. Applying the unitary transformation $U(t) = \exp(-i\frac{\omega_{21}t}{2}\sigma_z)$ to $\mathcal{H} = \mathcal{H}_q + \mathcal{H}_d$ evaluates to

$$\begin{aligned} \mathcal{H}' &= U \mathcal{H} U^\dagger - i\hbar U \dot{U}^\dagger \\ &\approx \frac{\hbar\Omega}{2} \sigma_x \end{aligned}$$

under the approximation that non-conserving energy terms $e^{\pm 2i\omega_{21}t}$ are neglected. The evolution of a ground state in this rotated frame is

$$\begin{aligned} U'(t) |0\rangle &= e^{-i\frac{\mathcal{H}'}{\hbar}t} |0\rangle \\ &= \cos(\Omega t/2) |0\rangle + i \sin(\Omega t/2) |1\rangle. \end{aligned}$$

Rabi oscillations are proportional to $\langle \sigma_- \rangle$ [4], $\sigma_- = |0\rangle \langle 1|$:

$$\begin{aligned} \langle \sigma_- \rangle &= \langle 0 | U'^\dagger(t) | 0 \rangle \langle 1 | U'(t) | 0 \rangle \\ &= \sin(\Omega t) \end{aligned}$$

-
- [1] Linke, Norbert M. and Maslov, Dmitri and Roetteler, Martin and Debnath, Shantanu and Figgatt, Caroline and Landsman, Kevin A. and Wright, Kenneth and Monroe, Christopher, Proceedings of the National Academy of Sciences, **114**, 3305-3310 (2017)
 - [2] John C Gitins, Multi-armed bandit allocation indices, Chichester, New York: Wiley, (1989)
 - [3] M. D. Reed, L. DiCarlo, S. E. Nigg, L. Sun, L. Frunzio, S. M. Girvin and R. J. Schoelkopf, Nature **482**, 382-385 (2011)
 - [4] O. Astafiev and A. M. Zagoskin and A. A. Abdumalikov and Yu. A. Pashkin and T. Yamamoto and K. Inomata and Y. Nakamura and J. S. Tsai, Science, **327**, 5967 (2010)
 - [5] Hoi, Io-Chun and Wilson, C. M. and Johansson,

- Göran and Palomaki, Tauno and Peropadre, Borja and Delsing, Per, Phys. Rev. Lett., **107**, 073601 (2011)
- [6] Hönigl-Decrinis T., Antonov I. V., Shaikhaidarov, R. and Antonov, V. N. and Dmitriev, A. Yu. and Astafiev, O. V., Phys. Rev. A, **98**, 041801 (2018)
- [7] Shen, Jung-Tsung and Fan, Shanhui, Phys. Rev. Lett, **95**, 213001 (2005)
- [8] M. W. Johnson and P. Bunyk and F. Maibaum and E. Tolkacheva and A. J. Berkley and E. M. Chapple and R. Harris and J. Johansson and T. Lanting and I. Perminov and E. Ladizinsky and T. Oh and G. Rose, Supercond. Sci. Technol., **23**, 065004 (2010)
- [9] Monroe, C. and Meekhof, D. M. and King, B. E. and Itano, W. M. and Wineland, D. J., Physical Review Letters, **75**, 4714 (1995)
- [10] , M. H. Devoret and A. Wallraff and J. M. Martinis (2008)
- [11] T.P. Orlando and J.E. Mooij and Lin Tian and Caspar H. van der Wal and L. Levitov and Seth Lloyd and J.J. Mazo, Science, **285**, 1036 (1999)
- [12] I. Chiorescu and Y. Nakamura and C. J. P. M. Harmans and J. E. Mooij, Science, **299**, 1869 (2003)
- [13] Mooij, J. E. and Orlando, T. P. and Levitov, L. and Tian, Lin and van der Wal, Caspar H. and Lloyd, Seth, Science, **285**, **5430** (1999)
- [14] A. Cottet, D. Vion, A. Aassime, P. Joyez, D. Esteve, M.H. Devoret, Physica C: Superconductivity, **367**, 197 (2002)
- [15] Gu, Xiu and Kockum, Anton Frisk and Miranowicz, Adam and Liu, Yu-xi and Nori, Franco, Physics Reports, **718-719**, 1–102 (2017)
- [16] Stern, M. and Catelani, G. and Kubo, Y. and Grezes, C. and Bienfait, A. and Vion, D. and Esteve, D. and Bertet, P., Phys. Rev. Lett., **113**, 123601 (2014)
- [17] Yan, Fei and Gustavsson, Simon and Kamal, Archana and Birenbaum, Jeffrey and Sears, Adam P and Hover, David and Gudmundsen, Ted J. and Rosenberg, Danna and Samach, Gabriel and Weber, S and Yoder, Jonilyn L. and Orlando, Terry P. and Clarke, John and Kerman, Andrew J. and Oliver, William D, Nature Communications, **7**, 12964 (2016)
- [18] Yueyin Qiu and Wei Xiong and Xiao-Ling He and Tie-Fu Li and J. Q. You, Scientific Reports, **6**, 28622 (2016)
- [19] Pop, Ioan M. and Geerlings, Kurtis and Catelani, Gianluigi and Schoelkopf, Robert J. and Glazman, Leonid I. and Devoret, Michel H., Nature, **508**, **369** (2014)
- [20] Zhu,Xiaobo and Kemp,Alexander and Saito,Shiro and Semba,Kouichi, Applied Physics Letters, **97**, **102503** (2010)
- [21] Original bad-ass paper
- [22] Yu-Lin Wu and Hui Deng and Hai-Feng Yu and Guang-Ming Xue and Ye Tian and Jie Li and Ying-Fei Chen and Shi-Ping Zhao and Dong-Ning Zheng, Chinese Physics B, **22**, 060309 (2013)
- [23] C T Earnest et al 2018 Supercond. Sci. Technol. **31** 125013
- [24] Barends,R. and Wenner,J. and Lenander,M. and Chen,Y. and Bialczak,R. C. and Kelly,J. and Lucero,E. and O'Malley,P. and Mariantoni,M. and Sank,D. and Wang,H. and White,T. C. and Yin,Y. and Zhao,J. and Cleland,A. N. and Martinis,John M. and Baselmans,J. J. A., Applied Physics Letters, **99**, 113507, 2011
- [25] Abdumalikov, A. A. and Astafiev, O. and Zagorskin, A. M. and Pashkin, Yu. A. and Nakamura, Y. and Tsai, J. S., Phys. Rev. Lett., **104**, 193601 (2010)
- [26] <https://arxiv.org/abs/cond-mat/0609441>
- [27] Vladimir E. Manucharyan and Jens Koch and Leonid I. Glazman and Michel H. Devoret, Science, **326**, 113 (2009)
- [28] Devitt, Simon J., Phys. Rev. A, **94**, 032329 (2016)
- [29] Gustavsson, S. and Bylander, J. and Yan, F. and Forn-Díaz, P. and Bolkhovsky, V. and Braje, D. and Fitch, G. and Harrabi, K. and Lennon, D. and Miloshi, J. and Murphy, P. and Slattery, R. and Spector, S. and Turek, B. and Weir, T. and Welander, P. B. and Yoshihara, F. and Cory, D. G. and Nakamura, Y. and Orlando, T. P. and Oliver, W. D., Phys. Rev. Lett., **108**, 170503(2012)
- [30] <http://microchem.com/pdf/PMGI-Resists-data-sheetV-rhcedit-102206.pdf>
- [31] <http://www.nanophys.kth.se/nanophys/facilities/nfl/resists/S1813/datasheet>